NeuroImage 254 (2022) 119135

Contents lists available at ScienceDirect

NeuroImage

journal homepage: www.elsevier.com/locate/neuroimage

Soma and Neurite Density MRI (SANDI) of the *in-vivo* mouse brain and comparison with the Allen Brain Atlas

Andrada Ianuş[a,*], Joana Carvalho[a], Francisca F. Fernandes[a], Renata Cruz[a], Cristina Chavarrias[a], Marco Palombo[b,c,d], Noam Shemesh[a,*]

[a] Champalimaud Research, Champalimaud Foundation, Av. Brasilia, Lisbon 1400-038, Portugal
[b] Center for Medical Image Computing, Department of Computer Science, University College London, UK
[c] Cardiff University Brain Research Imaging Centre, School of Psychology, Cardiff University, UK
[d] School of Computer Science and Informatics, Cardiff University, UK

A B S T R A C T

Diffusion MRI (dMRI) provides unique insights into the neural tissue milieu by probing interactions between diffusing molecules and tissue microstructure. Most dMRI techniques focus on white matter (WM) tissues, nevertheless, interest in gray matter characterizations is growing. The Soma and Neurite Density MRI (SANDI) methodology harnesses a model incorporating water diffusion in spherical objects (assumed to be associated with cell bodies) and in impermeable "sticks" (assumed to represent neurites), which potentially enables the characterization of cellular and neurite densities. Recognising the importance of rodents in animal models of development, aging, plasticity, and disease, we here employ SANDI for *in-vivo* preclinical imaging and provide a first validation of the methodology by comparing SANDI metrics with cellular density reflected by the Allen mouse brain atlas. SANDI was implemented on a 9.4T scanner equipped with a cryogenic coil, and *in-vivo* experiments were carried out on $N = 6$ mice. Pixelwise, ROI-based, and atlas comparisons were performed, magnitude vs. real-valued analyses were compared, and shorter acquisitions with reduced the number of b-value shells were investigated. Our findings reveal good reproducibility of the SANDI parameters, including the sphere and stick fractions, as well as sphere size (CoV < 7%, 12% and 3%, respectively). Additionally, we find a very good rank correlation between SANDI-driven sphere fraction and Allen mouse brain atlas contrast that represents cellular density. We conclude that SANDI is a viable preclinical MRI technique that can greatly contribute to research on brain tissue microstructure.

1. Introduction

The development of non-invasive imaging biomarkers which can reflect microscopic tissue properties, for instance the size and density of cells and/or neurite projections (Alexander et al., 2017; Novikov et al., 2019), is an active research topic for neuroimaging in general and diffusion Magnetic Resonance Imaging (dMRI) in particular. In dMRI, the signal is sensitized to micron-scale displacements of water molecules in the tissue, which are strongly influenced by microscopic boundaries imparted by cellular and subcellular structures (Stejskal and Tanner, 1965). Various approaches have been proposed for analysis of dMRI signals and a detailed discussion can be found in several excellent recent reviews (Alexander et al., 2017; Novikov et al., 2019; Novikov et al., 2018; Ghosh et al., 2018; Jelescu et al., 2020; De Luca et al., 2021). Among these approaches, *biophysical modeling* aims to disentangle signal contributions from two or more water pools, usually assigned to different tissue components, such as intra- and extracellular space (Alexander et al., 2017; Novikov et al., 2019, 2018; Ghosh et al., 2018; Jelescu et al., 2020; Panagiotaki et al., 2012). For instance, some techniques (Behrens et al., 2003; Jespersen et al., 2010, 2007; Zhang et al., 2012; Fieremans et al., 2013) model the signal ascribed to the intra-neurite space (i.e. axons and dendrites) by diffusion inside impermeable cylinders, usually considered to have zero radius (i.e. "sticks" (Behrens et al., 2007)). Other studies, consider the axon diameters finite and aim to estimate them, usually including measurements with high diffusion weighting (Stanisz et al., 1997; Assaf et al., 2008; Alexander et al., 2010; Kakkar et al., 2018; Huang et al., 2020; Fan et al., 2020; Veraart et al., 2020). Nevertheless, in most cases the extra-neurite tissue signal is assumed to comprise both spins in extra-cellular space as well as spins inside cell bodies, which are both modeled as a single, Gaussian diffusion system (Novikov et al., 2018; Panagiotaki et al., 2012; Jespersen et al., 2010, 2007; Fieremans et al., 2013; Behrens et al., 2007; Sotiropoulos et al., 2012; Kaden et al., 2016; Ferizi et al., 2014). To better capture the signal decay over a wide range of diffusion weightings up to high b-values, other techniques include an additional component comprising slow Gaussian diffusion (Olesen et al., 2021; Palombo et al., 2018; Tax et al., 2020). In some cases, the slow diffusion component is represented by restricted diffusion (Stanisz et al., 1997) in spheres (Palombo et al., 2018) and has been proposed to represent the signal from cell bodies (and other quasi spherical

* Corresponding authors.
E-mail addresses: Andrada.Ianus@neuro.fchampalimaud.org (A. Ianuş), Noam.Shemesh@neuro.fchampalimaud.org (N. Shemesh).

https://doi.org/10.1016/j.neuroimage.2022.119135.
Received 16 December 2021; Received in revised form 15 February 2022; Accepted 22 March 2022
Available online 23 March 2022.

structures), with a significant contribution especially in gray matter (GM) (Stanisz et al., 1997; Palombo et al., 2020; Afzali et al., 2021; Gyori et al., 2021).

The recently-introduced Soma and Neurite Density Imaging (SANDI) methodology (Palombo et al., 2020) aims to characterise such spherical object contributions using standard single diffusion encoding (SDE) dMRI, acquired with several shells (usually ≥5) up to (very) high b-values and powder-averaged data (Callaghan et al., 1979). The SANDI model relies on a three-compartment model consisting of sticks, spheres and isotropic Gaussian diffusion fitted to the powdered averaged data. Insofar, SANDI has been applied to *in-vivo* human brain imaging on a high-performance scanner, as well as *ex-vivo* in the mouse brain, where a preliminary comparison with histology data showed a good correlation between the soma signal fraction and signal intensity of DAPI stain, a marker for cell nuclei (Palombo et al., 2019). Nevertheless, estimating the signal fractions of diffusion restricted in sticks and spheres is challenging due to signal-to-noise and contrast-to-noise limitations as well as bias due to Rician noise floor (Fan et al., 2020; Afzali et al., 2021; Ianus et al., 2020).

In this study we aim to address several gaps in the evaluation and application of the original SANDI approach based on SDE acquisitions: (i) we investigate the stability of SANDI metrics in the mouse brain, *in-vivo* at 9.4T; (ii) we utilize the complex dMRI data to assess experimentally the effects of Rician noise floor on the SANDI parameters; and perhaps most importantly, (iii) we assess the correspondence of SANDI parameters to a histological proxy of cell density based on the Allen mouse brain atlas; (iv) lastly, we also investigate the possibility of fitting SANDI to a shorter protocol with less shells and a lower maximum b-value, and its impact on the estimated parameters.

2. Methods

2.1. In-vivo *MRI experiments*

All animal studies were approved by the competent institutional and national authorities and performed according to European Directive 2010/63.

In-vivo dMRI data was acquired from $N = 6$ C57BL/6 J mice (34 ± 5 weeks on a 9.4T Bruker Biospec scanner equipped with an 86 mm quadrature transmission coil and 4-element array reception cryocoil. Briefly, mice were induced with 5% isoflurane and maintained at 1.5–2%, and their temperature and breathing rate were continuously monitored.

Diffusion MRI datasets for SANDI were acquired using a PGSE-EPI sequence with the following parameters: TE = 36.8 ms, TR = 4 s, 4 averages, slice thickness = 0.4 mm, 35 slices, in plane resolution = 0.12×0.12 mm^2, FOV = 14.2×12 mm^2, matrix = 118×100, Partial Fourier = 1.35, per-slice triggering and with fat suppression. The EPI acquisition bandwidth was 375 kHz and data were acquired in a single shot.

Diffusion data has 8 shells with b-values of 1, 2.5, 4, 5.5, 7, 8.5, 10 and 12.5 ms/μm^2 and 40 directions each, uniformly distributed on a hemisphere following the directions from the manufacturer. The diffusion time $\Delta = 20$ ms was chosen to provide sensitivity for mapping apparent soma density according to previous simulation studies (Ianus et al., 2020), and the gradient duration $\delta = 5.5$ ms was chosen based on the maximum diffusion weighting given the hardware constraints ($G_{max} \sim 660$ mT/m). Acquisition time was ~ 2.5 h.

2.2. *Data pre-processing*

Complex data for each of the four receiver channels was processed in Matlab® (The MathWorks, Natick, MA, USA), unless otherwise specified. Complex data was denoised per channel using the MP-PCA approach (Veraart et al., 2016) (step 1) and corrected for ghosts (Buonocore and Gao, 1997) (step 2). Then, different channels were combined using an adaptive approach (Walsh et al., 2000) (step 3), real valued data was calculated based on low-pass filtering (Fan et al., 2020; Eichner et al., 2015) (step 4), and images were corrected for Gibbs ringing (Kellner et al., 2016) (step 5). The last step was to rigidly register images to the first set of b0-values (step 6). A detailed description of each step is presented in SI.

Finally, data was normalized by the mean b0 image and was averaged over directions for each shell.

2.2. *SANDI analysis*

The SANDI model assumes three compartments, namely intra-neurite signal modeled as diffusion inside impermeable sticks, intra-soma signal modeled as restricted diffusion inside spheres, and extracellular signal modeled as Gaussian diffusion, as illustrated in Fig. 1b. The powder-averaged normalized diffusion signal has thus the following expression:

$$\frac{\tilde{S}(b)}{S(0)} = f_{stick}\tilde{A}_{stick}(\mathrm{b}) + f_{shere}\tilde{A}_{sphere}(\mathrm{b}) + f_{ball}\tilde{A}_{ball}(\mathrm{b}), \quad (1)$$

where $f_{stick} + f_{sphere} + f_{ball} = 1$; $\tilde{A}_{stick}$ and $\tilde{A}_{sphere}$ are the normalized, directionally averaged signals for restricted diffusion within neurites and soma, respectively and $\tilde{A}_{ball}$ is the normalized, directionally averaged signal of the extra-cellular space. The specific expressions are given in SI.

The parameters estimated from the direction-averaged data are D_{stick}, D_{ball}, R_{sphere} as well as the signal fractions subject to the constraint $f_{stick} + f_{sphere} + f_{ball} = 1$. The bulk diffusivity inside the sphere is fixed to D_{sphere} 2 μm^2/ms (Harkins et al., 2011). The parameters are fitted using a Random Forest regression algorithm (*TreeBagger* Matlab®) with 200 trees and default parameters, trained on simulated data. Details are provided in SI.

This model formulation assumes negligible exchange between compartments and it does not explicitly account for size distributions or intra-compartment kurtosis, which is neglected in the Gaussian Phase Distribution approximation for the spherical compartment.

2.4. *Magnitude vs real data*

The Rician noise distribution in magnitude data can lead to parameter biases especially when including measurements with very high diffusion weighting (Fan et al., 2020; Afzali et al., 2021), as typically reached in SANDI. One way to reduce this bias is to model the Rician noise (Alexander et al., 2010) or, when complex data is available, to use the real part of the data instead (Fan et al., 2020; Eichner et al., 2015). In the first analysis, we investigate the effect of using magnitude or real data on the SANDI parameters. Subsequently, to minimize the effect of Rician noise (Fan et al., 2020; Eichner et al., 2015), we use parameters derived from real data.

2.5. *ROI analysis*

For each animal, representative regions of interest (ROI) were manually delineated in gray matter (GM) (cortex, thalamus, striatum, hippocampus), white matter (WM) (corpus callosum, internal capsule) and cerebrospinal fluid (CSF) regions, as illustrated in Fig. 1c.

The ROI analysis was employed to (i) analyse differences of SANDI parameters derived from magnitude and real data and to (ii) investigate parameter distributions across different ROIs and variability across animals.

2.6. *Comparison with the Allen Brain Atlas*

The next analysis focused on comparing SANDI parameters with the Allen mouse brain atlas (Wang et al., 2020). In the atlas, which is based on serial two-photon tomography, the image intensity generally reflects

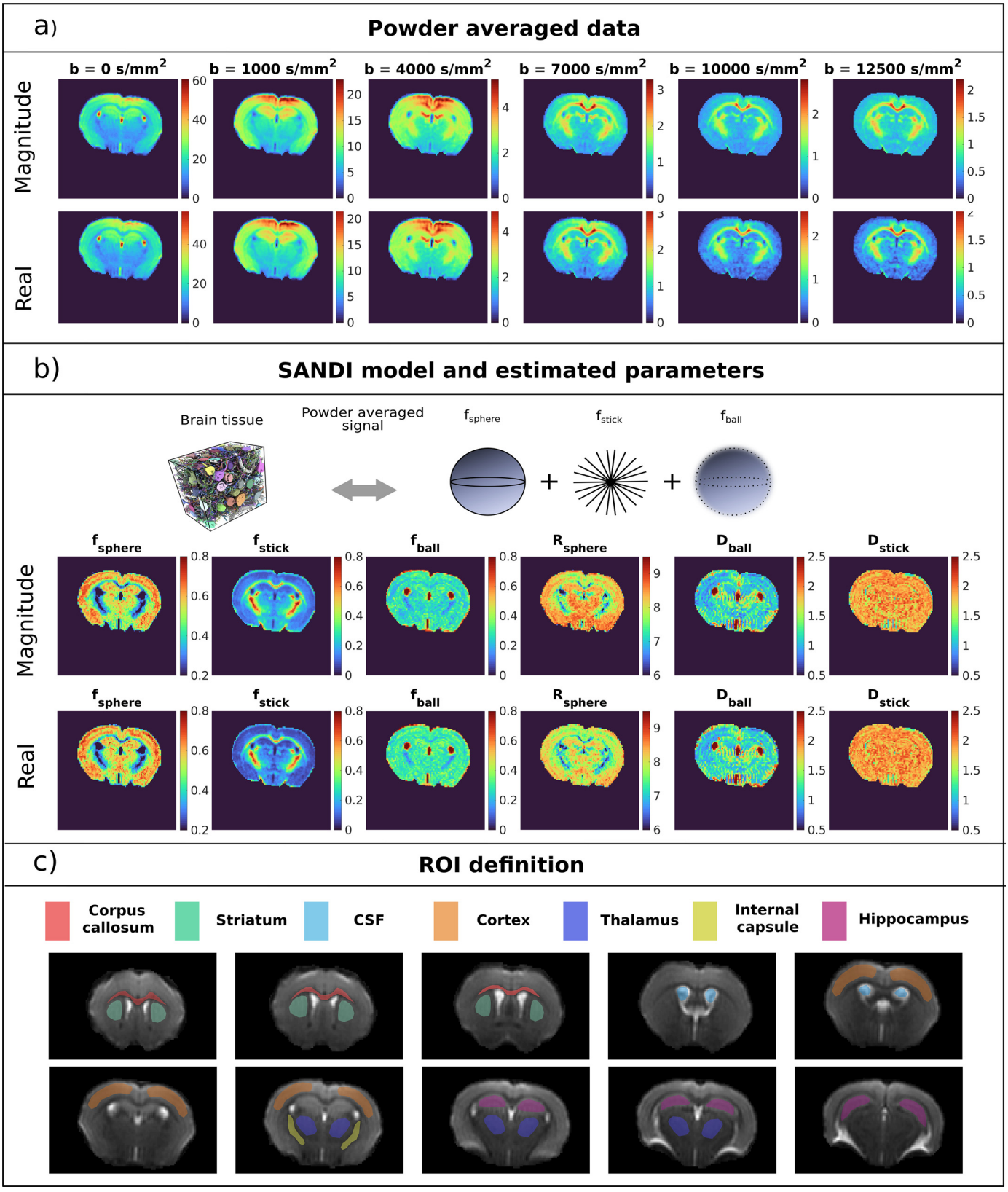

Fig. 1. (a) Powder-averaged raw diffusion weighted images using either magnitude or real data, from one representative animal. The data are presented for 6 different b values increasing left to right. Clearly, the signal to noise of the powder averaged data is high even at the highest b-value used in this study (b = 12.5 ms/μm^2), enabling the downstream processing of the SANDI model. The average SNR of the raw data across the entire brain was 37.9 ± 8.2, with higher values in GM, for instance SNR = 50.1 ± 12.7 in the cortex, and lower in WM, for instance SNR = 31.1 ± 5.2 in the internal capsule. After denoising the SNR increased by a factor of ~1.3. (b) SANDI parameter maps derived from magnitude (top) and real (bottom) data in one representative animal. Note the lower, but non-zero f_{sphere} in WM, and higher f_{sphere} in GM. The opposite is observed for f_{stick}. In the ventricles, f_{ball} is close to 1. Sphere radii are quite uniform across GM, and are lower in WM, while the diffusivity in sticks is between free diffusion (e.g. ventricles in D_{ball}) and the other Gaussian diffusion processes in the brain (D_{ball} in the brain parenhcyma).

cell density (Wang et al., 2020), with the exception of some highly cellular areas with large nuclei, such as the pyramidal layer of the hippocampus, a region excluded from the analysis.

2.6.1. Registration

To create the template, the P56 Mouse Brain Atlas in NIFTY format (https://scalablebrainatlas.incf.org/mouse/ABA_v3) was downsampled to match the resolution of the dMRI data, namely $0.12 \times 0.12 \times 0.4$ mm.

To compare the atlas intensity with SANDI parameters, we performed a 2D non-rigid registration (ANTs package (Avants et al., 2014)) on manually chosen slices to avoid interpolation between MRI slices during the registration process. We tested registrations both using $b = 0$ ms/μm^2 images as well as the f_{soma} maps, and the latter provided better outcomes. Then, the transformations were applied to all other parameters. The registered maps were then averaged over the 6 animals.

2.6.2. Correlation analysis

To study the link between the MRI derived parameters and the image intensity of the atlas, we considered WM and GM ROIs in three representative slices, covering the cerebrum and the cerebellum as illustrated in Fig. 4. Then, for all the voxels in the ROIs we computed the Spearman rank correlation coefficient (ρ) between the dMRI parameters and the atlas intensity, a metric that reflects a monotonic relationship between variables, rather than a linear relationship. The correlation coefficient was computed separately for WM and GM voxels, as well as for all voxels together.

2.7. Shorter acquisition protocols

The last analysis investigated how reducing SANDI's number of shells and maximum b-value affects the extracted metrics, aiming both to reduce the acquisition and to mimic weaker gradients, such as in more standard clinical scanners. Thus, we progressively excluded the last shells (higher b-values) from the full protocol employed in this study, which consists of 8 shells with a maximum b-value of 12.5 ms/μm^2. We have analysed data for 7 shells (b_{max} = 10 ms/μm^2), 6 shells (b_{max} = 8.5 ms/μm^2), and 5 shells (b_{max} = 7 ms/μm^2). Protocols with less than 5 shells were not tested as this is the number of free parameters in the current SANDI implementation. The RF regressors were retrained for each protocol.

3. Results

3.1. Data quality assessment

Fig. 1a depicts the registered, normalized and directionally averaged raw data. The maps show faster signal attenuation in GM compared to WM and clear white matter delineation at very high b-values ($b > 7$ ms/μm^2). Moreover, at high b-values we observe most differences between real and magnitude data due to the Rician noise floor. Fig. S1 presents similar plots for slices in the entire brain and Fig. S2 presents SNR maps. The observed superior-inferior image gradient is due to the sensitivity profile of the receiver cryoprobe (a 4-element arrayed surface coil).

3.2. SANDI parameter for magnitude and real data

Fig. 1b presents SANDI parameter maps for real and magnitude preprocessed data, in one representative animal. Overall, a good correspondence between parameters derived from real and magnitude data is observed, with better GM/WM contrast for real data. Maps of SANDI parameters for the entire brain are shown in Fig. S4 in Supplementary Information.

Fig. 2 depicts the correlation between parameters derived from magnitude and real data in different WM and GM ROIs. Overall, a good correlation was noted, especially for f_{stick} and D_{ball} with correlation coefficients $r > 0.8$. For f_{sphere} we also see high correlations in WM ($r > 0.85$), and slightly lower in GM ($0.5 < r < 0.8$). For R_{sphere} and f_{ball} the correlation strength is lower, especially in GM. In terms of bias, parameters estimated from magnitude data are slightly higher for f_{stick} and R_{sphere} and slightly lower for f_{sphere}, while other parameters show little bias, as also illustrated in the Bland-Altman diagrams in Fig. S3 in SI. The trends are consistent with simulations based on SANDI parameters from GM and WM when Gaussian or Rician noise was added (Fig. 2b).

3.3. SANDI parameter distributions within the ROIs

Next, we analyse SANDI metrics within similar GM, WM and CSF ROIs across the animals. Fig. 3a shows the powder-averaged signal decay from one voxel in each ROI, the prediction from the estimated SANDI parameters, as well as their difference, indicating a good model fit. Fig. 3b presents boxplots of the estimated SANDI parameters from ROI averaged signals and Fig. 3c presents the ROI distributions of SANDI parameters across animals, showing consistent values. Higher f_{sphere} values were observed in GM than in WM, while the f_{stick} contrast is reversed, consistent with previous results (Palombo et al., 2020; Afzali et al., 2021; Gyori et al., 2021). In CSF, both f_{sphere} and f_{stick} are almost 0 and f_{ball} is close to 1. The other parameters vary less across tissue ROIs. In CSF, D_{ball} approaches the diffusivity of free water. Table S1 in supplementary information presents the mean parameter values in each ROI.

The variability across animals was quantified by the coefficient of variation (CoV), calculated for the ROI averaged parameters as the ratio between the standard deviation and mean across animals. We found that f_{sphere} and f_{stick} have CoV values up to ~12% in tissue ROIs and higher in CSF due to the very low f_{sphere} and f_{stick} mean values. R_{sphere} and D_{stick} have low CoVs across animals (< 3.1% in tissue ROIs), while D_{ball} has higher values (6.4–15.4%). Intra-subject variability quantified from a bootstrapping analysis resulted in CoVs < 1.3% for all parameters, as detailed in SI.

3.5. Comparison of SANDI parameters with the Allen Brain Atlas

We then strived to compare SANDI parameters (f_{sphere}, f_{stick} and R_{sphere}) with the image intensity of the P56 Allen mouse brain atlas, which reflects cell density (among other things) (Wang et al., 2020). Fig. 4 shows the results for different ROIs in three representative slices covering the cerebrum (a) and cerebellum (b).

Group f_{sphere} maps qualitatively followed the intensity patterns observed in the downsampled Allen atlas in both cerebrum and cerebellum, with higher values in GM. Although group f_{sphere} does not exhibit the same dynamic range as the atlas image intensity in gray matter, it does provide contrast between different regions, for example it has lower values in striatum and amygdala compared to the cortex. When considering voxels in both GM and WM, the scatterplots show that there is a strong positive rank correlation between group f_{sphere} and the atlas intensity with Spearman correlation coefficients of ρ_t=0.71, ρ_t=0.72 and ρ_t=0.69, for ROIs in the three different slices. When considering the tissue types separately, we see lower correlation coefficients in GM compared to WM with ρ_{GM}= {0.53, 0.45, 0.59} and ρ_{WM}= {0.77, 0.69, 0.62} for the three different slices. Moreover, in two slices, the overall correlation coefficient is higher than the one measured for each tissue separately, showing that, as expected, the differences in f_{sphere} between WM and GM play an important role in the measured correlations.

When considering both GM and WM ROIs, we also see moderate negative correlations with f_{stick} (ρ_t=-0.47, ρ_t=-0.54, ρ_t =-0.53) and weak positive correlations with R_{sphere} (ρ_t =0.37, ρ_t =0.27, ρ_t =0.52). When analysing GM and WM ROIs separately, stronger correlations are usually observed for white matter voxels.

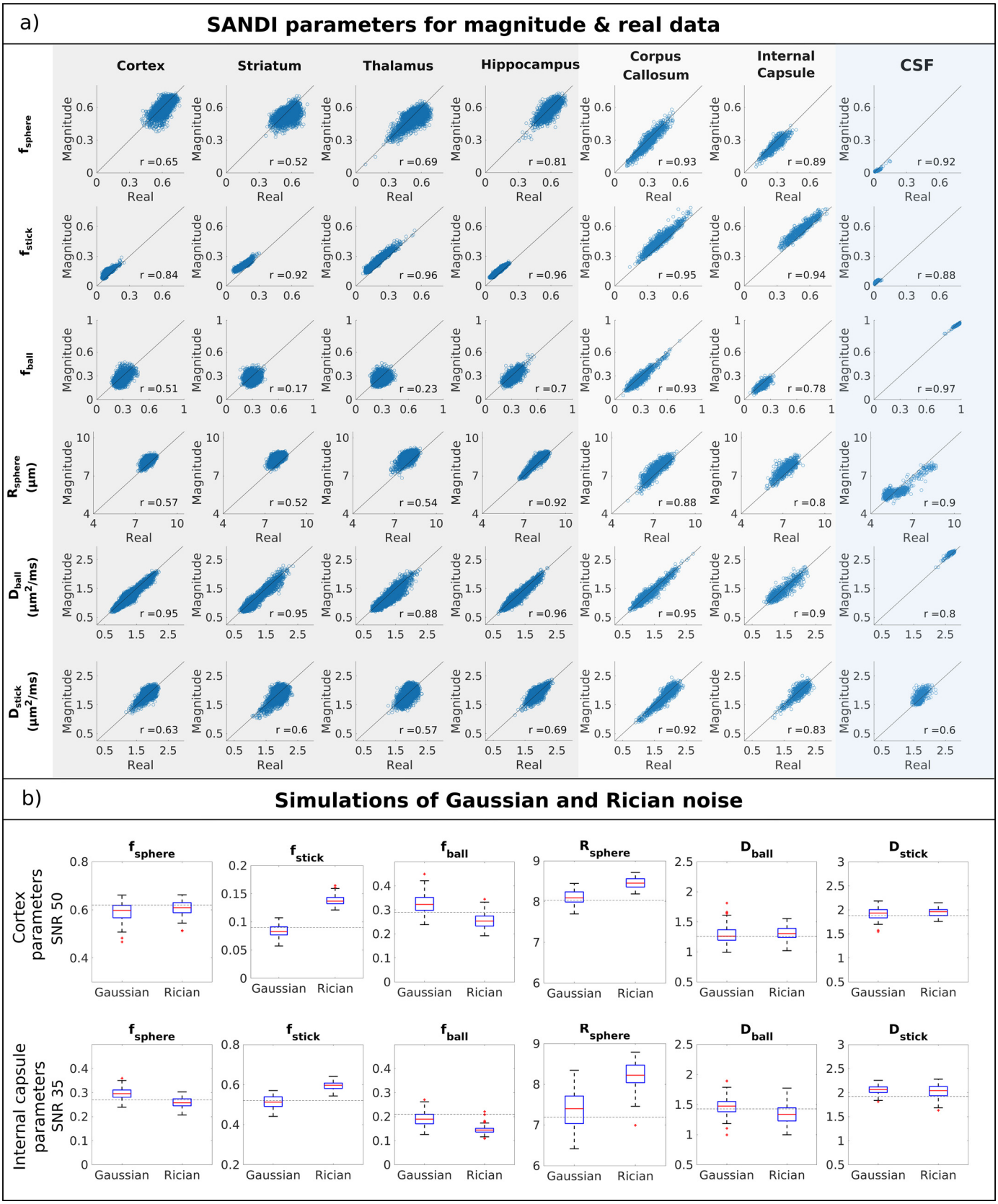

Fig. 2. (a) Scatter plots of SANDI parameters estimated based on real and magnitude data for the ROIs defined in Fig. 1c. The data is shown for GM ROIs (cortex, striatum, thalamus and hippocampus) depicted with dark gray, WM ROIs (corpus callosum and internal capsule) depicted with light gray, and CSF depicted with light blue. While correlations are generally good, some bias is observed in the magnitude data. All correlations are significant with $p << 0.01$. (b) Boxplots of estimated SANDI parameters based on simulated signals when either Gaussian or Rician noise is considered. The simulated signals are based on the average parameters values in the one GM ROI (cortex) and one WM ROI (internal capsule). To better mimic the effect of noise, the data was simulated for the different gradient directions, assuming a Watson distribution of sticks with concentration parameter of 0 in GM (i.e. isotropically distributed) and 10 in WM. Then Gaussian or Rician noise was added with an SNR of 50 in GM and 35 in WM, similar to the values we measured *in vivo*.

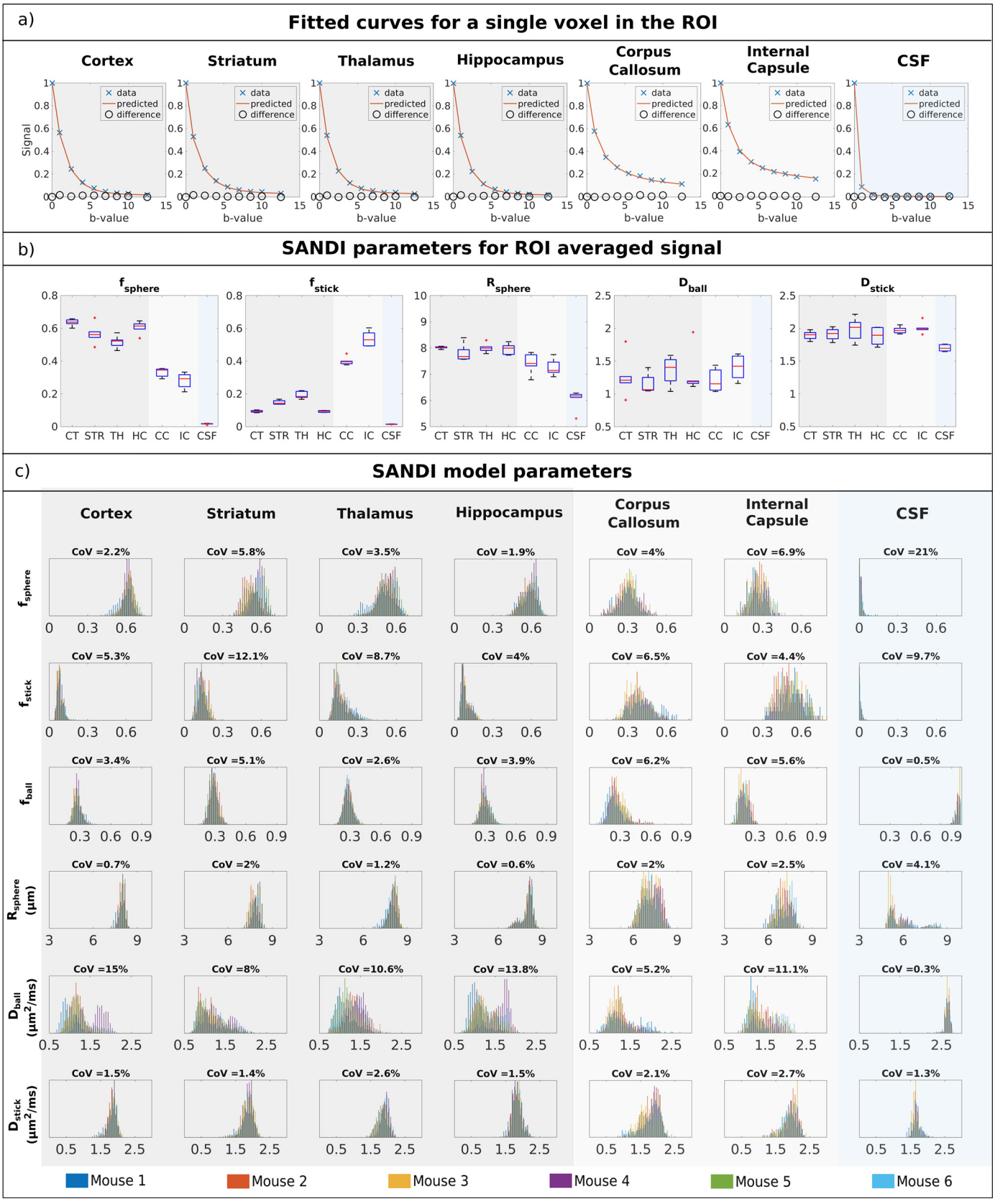

Fig. 3. (a) Decay curve as a function of *b*-value of the powder averaged signal, predicted signal from the estimated SANDI model parameters, as well as their difference for one voxel in GM, WM and CSF ROIs. The curves are presented for one representative animal and show a good fit of the SANDI model to the data. (b) Boxplots of estimated SANDI parameters across the six animals in the different ROIs calculated from the mean ROI signal. (c) Histograms of SANDI parameters in the different ROIs. The six animals are presented by different colours. The CoV across animals is calculated for the mean parameter values in each ROI. Excellent stability of the SANDI parameters is observed between the animals.

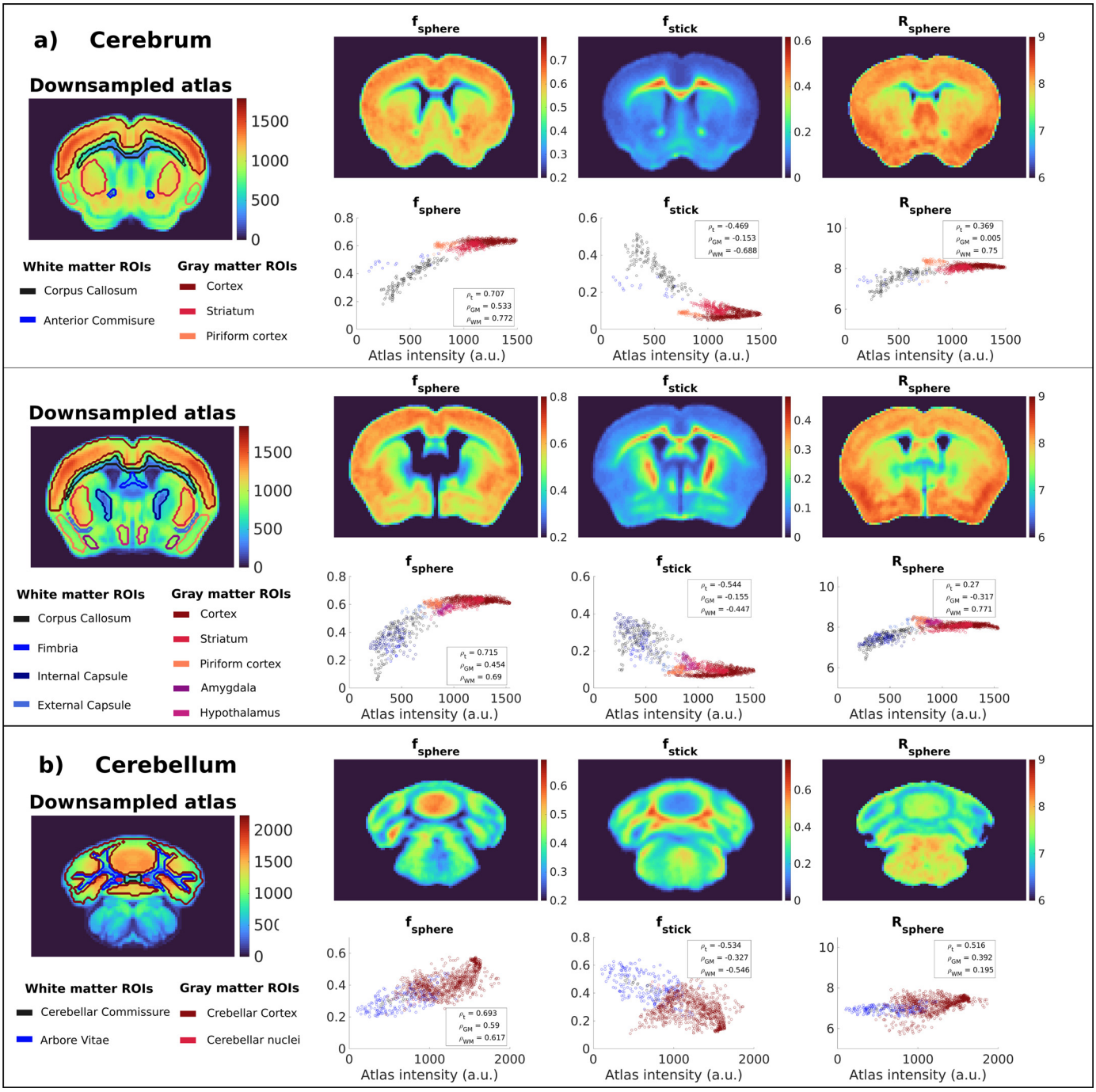

Fig. 4. Comparison between SANDI parameters and the downsampled Allen mouse brain atlas for three slices in the (a) cerebrum and (b) cerebellum. For each region, the top row shows the parameter maps derived from SANDI (f_{sphere}, f_{stick} and R_{sphere}) averaged over the 6 animals, after registration to the template as described in Section 2.6.2. The bottom row shows voxelwise scatter plots of the same parameters versus the image intensity of the atlas, for different GM and WM ROIs depicted on the downsampled atlas. The legend presents the Spearman correlation coefficients, derived for all voxels in the ROIs, for GM voxels and for WM voxels. All correlations with $|\rho| > 0.1$ are significant with $p << 0.01$. Strikingly, f_{sphere} exhibits a very good rank correlation with the Allen brain contrast in both cerebrum and cerebellum.

Similar patterns were observed in individual mice, as illustrated in Fig. S5.

3.7. Shorter SANDI protocols

Finally, we investigated the potential of using SANDI acquisitions with less shells and lower maximum b-values. Fig. 5 illustrates the SANDI parameters estimated from protocols with 8, 7, 6 and 5 shells, revealing that the values are overall stable, both in terms of median values and interquartile ranges, which reflect variability within the ROIs as well as between animals. In most cases presented in Fig. 5, the median values estimated from the 5-shell protocol are within 10% of the values estimated from the full protocol (dotted green lines). In other cases, there is a small change in parameter values, for instance, an increase in the estimated R_{sphere}, which is more pronounced in the WM ROIs, as well as an increase in f_{stick} in the GM ROIs. For R_{sphere}, the median values are

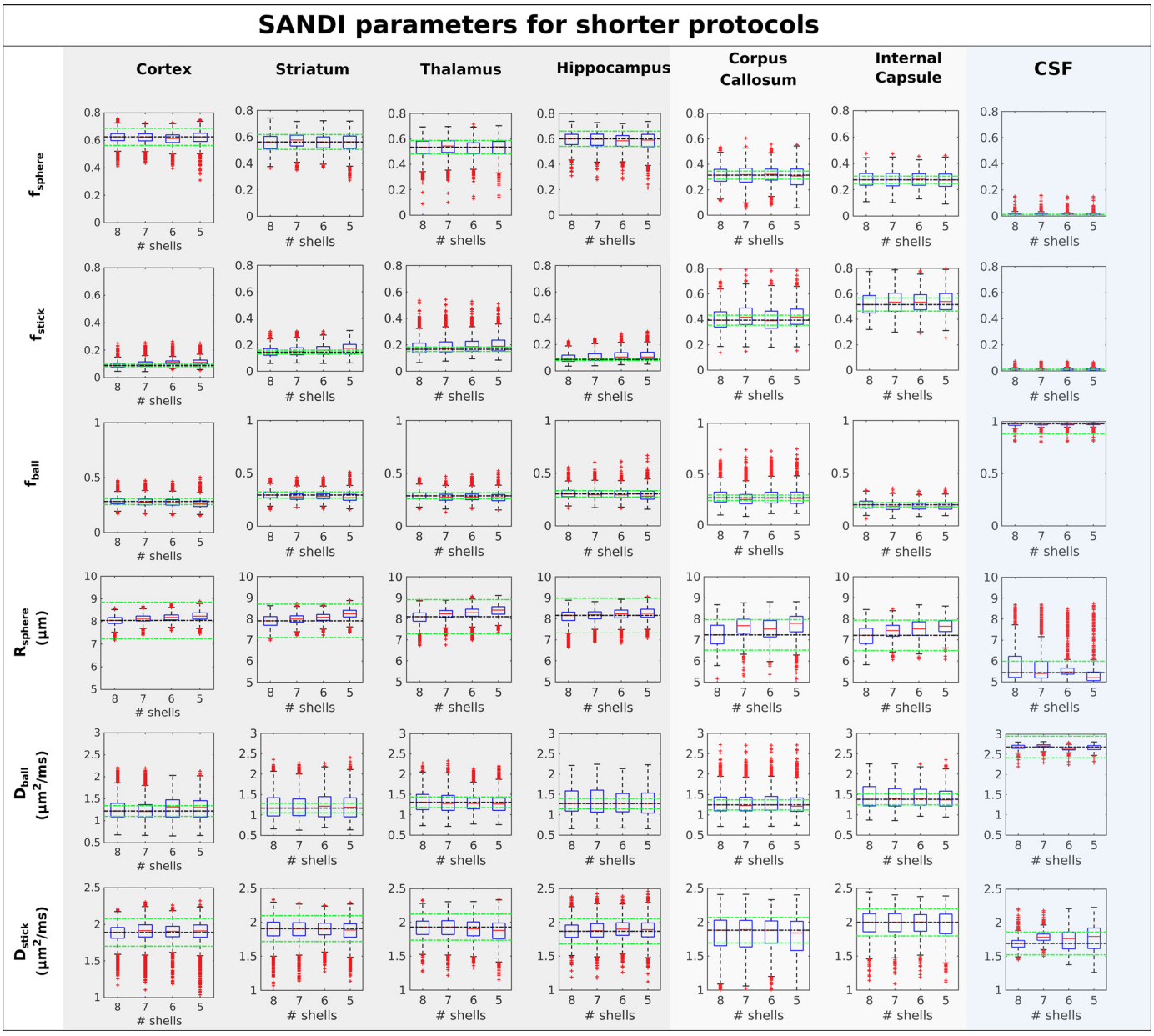

Fig. 5. Boxplots of estimated SANDI parameters for protocols with varying number of shells in GM, WM, and CSF ROIs. The parameters are estimated voxelwise and aggregated over different animals for the voxels in each ROI. The rows present different model parameters and the columns different ROIs. The dotted black lines show the values estimated from the full, 8-shell, protocol, while the green lines show a variation of ±10% from this value. The b-values employed in the different protocols are the following: full protocol (8 shells): b = {1, 2.5, 4, 5.5, 7, 8.5, 10, 12.5} ms/μm^2; 7-shells: b = {1, 2.5, 4, 5.5, 7, 8.5, 10} ms/μm^2; 6-shells: b = {1, 2.5, 4, 5.5, 7, 8.5} ms/μm^2 and 5-shells: b = {1, 2.5, 4, 5.5, 7} ms/μm^2. Overall, all SANDI parameters are stable as the protocol is reduced from 8 shells with maximum b-value of 12.5 ms/μm^2 to 5 shells with maximum b-value of 7 ms/μm^2.

still within 10% difference, while for f_{stick} the absolute differences are small, i.e. median value differences < 0.03, although in GM this change is larger than 10% due to the overall small values of the parameters.

4. Discussion

In this work, we assessed the SANDI methodology for characterising mouse brain tissue microstructure, *in-vivo*. Specifically, we investigated the effect of Rician noise on the estimated parameters, the reproducibility across animals, the feasibility of using shorter protocols, as well as a first level validation by comparing the SANDI metrics with the intensity of the Allen Mouse Brain Atlas.

From a methodological perspective, we note that real valued data provides a robust and reproducible assessment of the SANDI parameters, even for shorter protocols. Our findings are in good agreement with previous *ex-vivo* SANDI-driven maps in the mouse brain (Palombo et al., 2020, 2019), and *in-vivo* SANDI maps in the human brain (Palombo et al., 2020; Afzali et al., 2021; Gyori et al., 2021). Notably, the sphere fraction is close to zero in CSF (especially when using real-valued data) and intermediate (~0.3) in WM, likely reflecting the non-negligible (Palombo et al., 2019; Sampaio-Baptista and Johansen-Berg, 2017) WM cell body population (neurons, astrocytes, microglia) in WM. The largest f_{sphere} estimates were observed in GM with values between 0.45 and 0.65. When considering the cell densities and sizes measured from histology (Keller et al., 2018; Palombo et al., 2021), a

lower bound on cell body volume fraction can be considered in the range 12–40% for different GM areas. The higher f_{sphere} values estimated by SANDI (~45–65%) can also be explained by the fact that f_{sphere} is a signal fraction and not a volume fraction, hence also affected by relaxation effects (e.g., T1, T2). Although previous *ex-vivo* SANDI data acquired with much higher spatial resolution ($0.05 \times 0.05 \times 0.25$ mm^3) was able to capture f_{sphere} differences between GM cortical layers (Palombo et al., 2019), here, such differences were not as obvious, likely due to the lower spatial resolution ($0.12 \times 0.12 \times 0.4$ mm^3). Furthermore, the coefficients of variation of the mean f_{sphere} values across animals were small, < 8% both in GM and WM, suggesting a good reproducibility of SANDI metrics.

SANDI-driven R_{sphere} values exhibited lower values in WM compared with GM. Overall, the estimated R_{sphere} values are between 6 and 9 μm, approximately consistent with values derived from histology (Erö et al., 2018), considering that the apparent effective radii are tail-weighted values of the underlying distribution of sizes (Palombo et al., 2021) (c.f. Fig. S7 for simulations). Larger R_{sphere} values can also be observed in regions known to have larger cells, such as the granular and pyramidal layer of the hippocampus or the piriform cortex (Paxinos and Franklin, 2019) (Fig. S6). Nevertheless, for a detailed analysis of R_{sphere} and soma sizes, further experiments comparing MRI and histology are needed. The choice of sequence parameters, especially the gradient duration and diffusion time, can also play a role on the sensitivity to different cellular sizes and might influence the estimated R_{sphere} values, especially in the presence of exchange.

Neurites in SANDI are modeled as cylinders with zero radius (i.e. sticks) (Jespersen et al., 2010, 2007; Zhang et al., 2012; Fieremans et al., 2013; Behrens et al., 2007). When considering the possibility of non-zero cylinder radii, the estimated f_{stick} and D_{stick} values are stable for R_{cyl} < 1.5 μm, which is plausible for most WM, although, the parameters can become biased for larger axons as illustrated in Fig. S7 and consistent with previous literature (Fan et al., 2020; Drobnjak et al., 2015). The coefficient of variation for f_{stick} is also relatively small < 12% and the patterns and values of f_{stick} measured here are in line with previous works estimating the signal fraction of sticks from directional data (Jespersen et al., 2010, 2007; Zhang et al., 2012; Fieremans et al., 2013), as well as powder averaged data (Palombo et al., 2020, 2019; Afzali et al., 2021; Gyori et al., 2021). The other SANDI parameters, namely D_{ball} and D_{stick} were also quite reproducible across animals, although their fits seem to better capture imaging artifact effects, for instance Gibbs ringing around the ventricles, that were not fully corrected due to the partial Fourier acquisition, as also observed before with diffusion metrics (Guglielmetti et al., 2016).

From a more biological perspective, we attempted to correlate the SANDI contrasts with the Allen mouse brain contrast which reflects to some extent cell density (Wang et al., 2020). Interestingly, SANDI-driven f_{sphere} was the only parameter that was strongly correlated with the Allen mouse brain atlas image intensity, suggesting that – whether directly or indirectly – f_{sphere} is influenced, at least in part, by cell body density. Similar correlation patterns were observed even in individual animals (Fig. S5) which bodes well for future individual animal characterizations in health and disease.

Although we find a strong rank correlation between f_{sphere} and the Allen mouse brain atlas when including both white matter and gray matter voxels, we observe only a moderate correlation in gray matter, where the atlas exhibits a wider dynamic range of intensity values compared to f_{sphere}. This is likely due to the different contrast mechanisms of the two imaging modalities. In Allen atlas' two-photon tomography, the image intensity is related to the amount of cytoplasm, while f_{sphere} reflects the amount of dMRI signal arising from water molecules restricted in spherical environments. While both metrics are considered to reflect to some extent cell density, their contrast is inherently different. One example is the hippocampus, where the pyramidal layer has highly packed cells, as illustrated by stains such as Nissl (Paxinos and Franklin, 2019). However, in the Allen Brain Atlas, the pyramidal layer appears dark, due to the large and densely packed cell nuclei. Nevertheless, SANDI's f_{sphere} is high in this region as expected. These findings are encouraging for future studies more directly correlating specific aspects of the microstructure with more refined SANDI theory, e.g., including exchange (Olesen, 2022; Jelescu et al., 2021) (see below).

4.1. Limitations

As any study, several limitations can be identified in our work. First, the SANDI model assumptions include non-exchanging compartments, spherical structures, sticks, and a well-mixed extracellular environment characterised by Gaussian diffusion. These assumptions are likely overly simplified and do not account for the tissue's complexity. Variations in cell sizes and shapes, finite neurite sizes, intracellular organelles, membrane permeability and exchange across different compartments, etc., can all bias SANDI's estimations and the interpretation of its metrics. Further, kurtosis of each compartment is assumed negligible, in contrast with recent clinical and pre-clinical Correlation Tensor MRI studies (Henriques et al., 2020, 2021; Novello et al., 2022). In addition, recent studies suggest that water exchange across compartments can be faster in GM and can influence the dMRI signal at this diffusion time (Olesen et al., 2022; Jelescu et al., 2021; Lee et al., 2020), while others have shown that the intra-cellular residence time of water is on the order of 500 ms (Yang et al., 2018), a timescale that would not render an important mechanism at the diffusion time considered here (20 ms). Future work should aim at incorporating exchange to the model (Olesen et al., 2022), and harnessing multiple diffusion times, e.g. between 10 and 40 ms for pre-clinical acquisition, to disentangle the effects.

The comparison of SANDI metrics with the Allen mouse brain atlas contrast is clearly confounded by the different sources of information, the usage of averaged-brain templates, and different inherent spatial resolution. Future studies should be performed using individual-level comparisons, where SANDI maps will be compared to maps derived from directly targeted histology mapping cell body density.

Data availability

The data sets generated and analysed during the current study are available on OpenNeuro: https://openneuro.org/datasets/ds003959/versions/1.0.1.

Code availability

SANDI code is available on GitHub at https://github.com/palombom.

Credit authorship contribution statement

Andrada Ianuş: Conceptualization, Data curation, Formal analysis, Funding acquisition, Investigation, Methodology, Project administration, Resources, Software, Supervision, Visualization, Writing – original draft, Writing – review & editing. **Joana Carvalho:** Software, Funding acquisition, Writing – review & editing. **Francisca F. Fernandes:** Funding acquisition, Writing – review & editing. **Renata Cruz:** Funding acquisition. **Cristina Chavarrias:** Funding acquisition, Project administration. **Marco Palombo:** Conceptualization, Funding acquisition, Methodology, Software, Writing – review & editing. **Noam Shemesh:** Conceptualization, Funding acquisition, Investigation, Methodology, Project administration, Resources, Software, Supervision, Visualization, Writing – review & editing.

Acknowledgments

This study was funded by the European Research Council (ERC) under the European Union's Horizon 2020 research and innovation programme (Starting Grant, agreement No. 679058). The authors acknowl-

edge the vivarium of the Champalimaud Center for the Unknown, a facility of CONGENTO financed by Lisboa Regional Operational Programme (Lisboa 2020), project LISBOA01-0145-FEDER-022170. AI and RC are supported by "la Caixa" Foundation (ID 100010434) and from the European Union's Horizon 2020 research and innovation programme under the Marie Skłodowska-Curie grant agreement No 847648, fellowship code CF/BQ/PI20/11760029. JC is supported by ERC (Starting Grant, agreement No. 679058) and by European Union's Horizon 2020 research and innovation programme under the Marie Sklodowska-Curie grant agreement No 101032056. MP is supported by UKRI Future Leaders Fellowship grant no. MR/T020296/2.

Supplementary materials

Supplementary material associated with this article can be found, in the online version, at doi:10.1016/j.neuroimage.2022.119135.

References

Afzali, M., et al., 2021. SPHERIOUSLY? The challenges of estimating sphere radius non-invasively in the human brain from diffusion MRI. Neuroimage 237, 118183.
Alexander, D.C., et al., 2010. Orientationally invariant indices of axon diameter and density from diffusion MRI. Neuroimage 52 (4), 1374–1389.
Alexander, D.C., et al., 2017. Imaging brain microstructure with diffusion MRI: practicality and applications. NMR Biomed. 32 (4), e3841.
Assaf, Y., et al., 2008. AxCaliber: a method for measuring axon diameter distribution from diffusion MRI. Magn. Reson. Med. 59, 1347–1354.
Avants, B.B., et al., 2014. The insight ToolKit image registration framework. Front. Neuroinform. 8, 44 -44.
Behrens, T.E., et al., 2003. Characterization and propagation of uncertainty in diffusion-weighted MR imaging. Magn. Reson. Med. 50, 1077–1088.
Behrens, T.E., et al., 2007. Probabilistic diffusion tractography with multiple fibre orientations: what can we gain? Neuroimage 34 (1), 144–155.
Buonocore, M.H., Gao, L., 1997. Ghost artifact reduction for echo planar imaging using image phase correction. Magn. Reson. Med. 38 (1), 89–100.
Callaghan, P.T., Jolley, K.W., Lelievre, J., 1979. Diffusion of water in the endosperm tissue of wheat grains as studied by pulsed field gradient nuclear magnetic resonance. Biophys. J. 28 (1), 133–141.
De Luca, A., et al., On the generalizability of diffusion MRI signal representations across acquisition parameters, sequences and tissue types: chronicles of the MEMENTO challenge. bioRxiv, 2021: p. 2021.03.02.433228.
Drobnjak, I., et al., 2015. PGSE, OGSE, and sensitivity to axon diameter in diffusion MRI: insight from a simulation study. Magn. Reson. Med. 75, 688–700.
Eichner, C., et al., 2015. Real diffusion-weighted MRI enabling true signal averaging and increased diffusion contrast. Neuroimage 122, 373–384.
Erö, C., et al., 2018. A cell atlas for the mouse brain. Front. Neuroinform. 12, 84.
Fan, Q., et al., 2020. Axon diameter index estimation independent of fiber orientation distribution using high-gradient diffusion MRI. Neuroimage 222, 117197.
Ferizi, U., et al., 2014. A ranking of diffusion MRI compartment models with *in vivo* human brain data. Magn. Reson. Med. 72 (6), 1785–1792.
Fieremans, E., et al., 2013. Novel white matter tract integrity metrics sensitive to Alzheimer disease progression. AJNR Am. J. Neuroradiol. 34 (11), 2105–2112.
Ghosh, A., Ianus, A., Alexander, D.C., 2018. Advanced diffusion models. Quantitative MRI of the Brain, Principles of Physical Measurement, 2nd ed. M. Cercignani, N.G. Dowell, and T.P. S, Editors.
Guglielmetti, C., et al., 2016. Diffusion kurtosis imaging probes cortical alterations and white matter pathology following cuprizone induced demyelination and spontaneous remyelination. Neuroimage 125, 363–377.
Gyori, N.G., et al., 2021. On the potential for mapping apparent neural soma density via a clinically viable diffusion MRI protocol. Neuroimage 239, 118303.
Harkins, K.D., et al., 2011. Changes in intracellular water diffusion and energetic metabolism in response to ischemia in perfused C6 rat glioma cells. Magn. Reson. Med. 66 (3), 859–867.
Henriques, R.N., Jespersen, S.N., Shemesh, N., 2020. Correlation tensor magnetic resonance imaging. Neuroimage 211, 116605.
Henriques, R.N., et al., 2021. Evidence for microscopic kurtosis in neural tissue revealed by correlation tensor MRI. Magnetic Resonance in Medicine 86 (6), 3111–3130. doi:10.1002/mrm.28938.
Huang, S.Y., et al., 2020. High-gradient diffusion MRI reveals distinct estimates of axon diameter index within different white matter tracts in the *in vivo* human brain. Brain Struct. Funct. 225 (4), 1277–1291.
Ianus, A., et al., Mapping complex cell morphology in the grey matter with double diffusion encoding MRI: a simulation study. arXiv, 2020: p. 2009.11778.
Jelescu, I.E., et al., 2020. Challenges for biophysical modeling of microstructure. J. Neurosci. Methods, 108861.
Jelescu, I.E., et al., Neurite exchange imaging (NEXI): a minimal model of diffusion in gray matter with inter-compartment water exchange. https://arxiv.org/abs/2108.06121, 2021.
Jespersen, S.N., et al., 2007. Modeling dendrite density from magnetic resonance diffusion measurements. Neuroimage 34 (4), 1473–1486.
Jespersen, S.N., et al., 2010. Neurite density from magnetic resonance diffusion measurements at ultrahigh field: comparison with light microscopy and electron microscopy. Neuroimage 49 (1), 205–216.
Kaden, E., et al., 2016. Multi-compartment microscopic diffusion imaging. Neuroimage 139, 346–359.
Kakkar, L.S., et al., 2018. Low frequency oscillating gradient spin-echo sequences improve sensitivity to axon diameter: an experimental study in viable nerve tissue. Neuroimage 182, 314–328.
Keller, D., Erö, C., Markram, H., 2018. Cell densities in the mouse brain: a systematic review. Front. Neuroanat. 12.
Kellner, E., et al., 2016. Gibbs-ringing artifact removal based on local subvoxel-shifts. Magn. Reson. Med. 76, 1574–1581.
Lee, H.H., et al., 2020. *In vivo* observation and biophysical interpretation of time-dependent diffusion in human cortical gray matter. Neuroimage 222, 117054.
Novello, L., et al., 2022. In vivo Correlation Tensor MRI reveals microscopic kurtosis in the human brain on a clinical 3T scanner. NeuroImage, 119137 doi:10.1016/j.neuroimage.2022.119137.
Novikov, D.S., Kiselev, V.G., Jespersen, S.N., 2018. On modeling. Magn. Reson. Med. 79 (6), 3172–3193.
Novikov, D.S., et al., 2019. Quantifying brain microstructure with diffusion MRI: theory and parameter estimation. NMR Biomed. 32 (4), e3998.
Olesen, J.L., et al., 2021. Beyond the diffusion standard model in fixed rat spinal cord with combined linear and planar encoding. Neuroimage 231, 117849.
Olesen, J.L., et al., 2022. Diffusion time dependence, power-law scaling, and exchange in gray matter. Neuroimage, 118976.
Palombo, M., et al., 2018. Abundance of cell bodies can explain the stick model's failure in grey matter at high bvalue. In: Proceedings of the Joint Annual Meeting ISMRM-ESMRMB. Paris, France.
Palombo, M., et al., 2019. Histological validation of the brain cell body imaging with diffusion MRI at ultrahigh field. In: Proceedings of the ISMRM Annual Meeting. Montreal, Canada.
Palombo, M., et al., 2020. SANDI: a compartment-based model for non-invasive apparent soma and neurite imaging by diffusion MRI. Neuroimage 215, 116835.
Palombo, M., Alexander, D.C., Zhang, H., 2021. Large-scale analysis of brain cell morphometry informs microstructure modelling of gray matter. Proc. Int. Soc. Mag. Reson. Med. 29.
Panagiotaki, E., et al., 2012. Compartment models of the diffusion MR signal in brain white matter: a taxonomy and comparison. Neuroimage 59 (3), 2241–2254.
Paxinos, G., Franklin, K., 2019. The Mouse Brain in Stereotaxic Coordinates, 5th ed. Academic Press.
Sampaio-Baptista, C., Johansen-Berg, H., 2017. White matter plasticity in the adult brain. Neuron 96 (6), 1239–1251.
Sotiropoulos, S.N., Behrens, T.E., Jbabdi, S., 2012. Ball and rackets: inferring fiber fanning from diffusion-weighted MRI. Neuroimage 60 (2), 1412–1425.
Stanisz, G.J., et al., 1997. An analytical model of restricted diffusion in bovine optic nerve. Magn. Reson. Med. 37, 103–111.
Stejskal, E.O., Tanner, J.E., 1965. Spin diffusion measurements: spin echoes in the presence of a time-dependent field gradient. J. Chem. Phys. 42 288–+.
Tax, C.M.W., et al., 2020. The dot-compartment revealed? Diffusion MRI with ultra-strong gradients and spherical tensor encoding in the living human brain. Neuroimage 210, 116534.
Veraart, J., et al., 2016. Denoising of diffusion MRI using random matrix theory. Neuroimage 142, 394–406.
Veraart, J., et al., 2020. Noninvasive quantification of axon radii using diffusion MRI. Elife 9, e49855.
Walsh, D.O., Gmitro, A.F., Marcellin, M.W., 2000. Adaptive reconstruction of phased array MR imagery. Magn. Reson. Med. 43 (5), 682–690.
Wang, Q., et al., 2020. The allen mouse brain common coordinate framework: a 3D reference atlas. Cell 181 (4), 936–953 e20..
Yang, D.M., et al., 2018. Intracellular water preexchange lifetime in neurons and astrocytes. Magn. Reson. Med. 79 (3), 1616–1627.
Zhang, H., et al., 2012. NODDI: practical *in vivo* neurite orientation dispersion and density imaging of the human brain. Neuroimage 61 (4), 1000–1016.